Available online at www.sciencedirect.com
ScienceDirect
Applied Thermal Engineering 00 (2015) 1–16
Applied Thermal Engineering

CFD model of a moderator tank for a pressure vessel PHWR nuclear power plant

Santiago F. Corzo[a,b], Damian E. Ramajo[a], Norberto M. Nigro[a]

[a]*Research center for Computational Methods CIMEC-UNL-CONICET, Colectora ruta 168, km 472, paraje el pozo (3000) Santa Fe, Argentina, (+54-342-4511594).*
[b]*Nuclear Regulatory Authority ARN, Av. Libertador 8250 (C1428BNP) Buenos Aires, Argentina.*

Abstract

The CFD thermal hydraulic simulation of a Pressurized Heavy Water REactor (PHWR) moderator tank was performed. Heating was achieved by considering two heat sources, conduction/convection through the coolant channels and neutron thermalization. For the first method, a suitable 2D model for coupling the 3D with a 1D code to solve the in-channel coolant was implemented. For thermalization, a volumetric heat source was estimated. Due to the relevance of natural and forced convection in the heat transfer, the Boussinesq approach was assessed for high Rayleigh number flow before it was used to model the moderator tank. The results clarified the complex flow behaviour and the temperature field. It was noted that the thermal power transferred from the coolant was not directly related to the fission power distribution but to the coolant temperature profile (nearly the same for all channels) and the non-homogeneous moderator temperature. The former profile was as expected for high-Rayleigh natural convection flows.

Keywords: CFD, Heat Transfer, High Rayleigh number

☆

Email address: santiagofcorzo@gmail.com (Santiago F. Corzo)
URL: http://www.cimec.org.ar/twiki/bin/view/Cimec/ (Santiago F. Corzo)

1. Introduction

The Nuclear Power Plant (NPP) Atucha II is a Pressurized Heavy Water Reactor (PHWR) with a thermal power of 2160 and an electric power of 745 MW. It uses natural uranium (U_2O) and heavy water (D_2O) for moderating and cooling. The reactor has a Pressure Vessel (RPV) that housing 451 vertical Coolant Channels (CC) across the moderator tank. Thus, the coolant flows inside the CCs while the moderator flow floods outside them (see Figure 1). The CCs are arranged in a 272 mm trigonal lattice pitch, and each fuel bundle is composed of an assembly of 37 fuel rods with 5.3 m active length.

Inside the RPV, the coolant circuit is primarily composed of two large reservoirs; the cold one accounts for the downcomer annulus joined to the lower plenum. The hot one accounts for the upper plenum. The lower plenum houses the bottom ends of the CC (inlets throttles) while the upper plenum houses the top ends of the CC (outlet throttles). These two reservoirs are mainly connected through the CCs. However, for cooling purposes, a small amount of coolant (less than 3%) passes from the downcomer to the filler bodies located above the upper plenum.

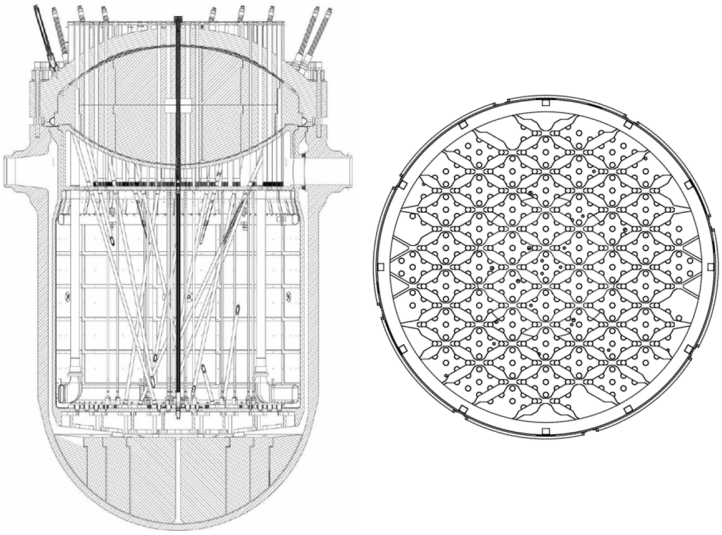

Figure 1. Cut view of the RPV.

Figure 1 presents a cross sectional view combining two cut planes to visualize one hot leg and one cold leg. The coolant enters the RPV through two cold legs and travels down towards the lower plenum through the thin annular downcomer bounded between the RPV outer wall and the moderator tank. Inside the lower plenum, there is a rhomboidal distributor that distributes the coolant to all of the CC inlets. Then, the coolant flows upward through the CCs extracting the fission heat until it is collected in the upper plenum. Lastly, it leaves the RPV through two hot legs.

The moderator tank is found in the central part of the RPV. In normal operation, the cold moderator enters the tank through four vertical downcomers, which are connected to a sparger ring placed at the bottom side of the tank. The ring has a set of mouthpieces and small orifices to distribute the flow. The moderator is heated by the heat transferred from the coolant channels and neutron thermalization. Lastly, the hot moderator is collected at the top of the tank using a perforated collector ring. In Atucha II, the moderator tank is the first heat sink under a Loss Of Coolant Accident (LOCA).

Outside the RPV, the primary circuit is composed of two loops that transport the heat from the core to the light-water (H_2O) secondary circuit in the steam generators (see Figure 2[1]). The moderator circuit is composed of four interconnected loops, each compromising a heat exchanger and a pump.

[1] Figure courtesy of Bonelli et al.[1]

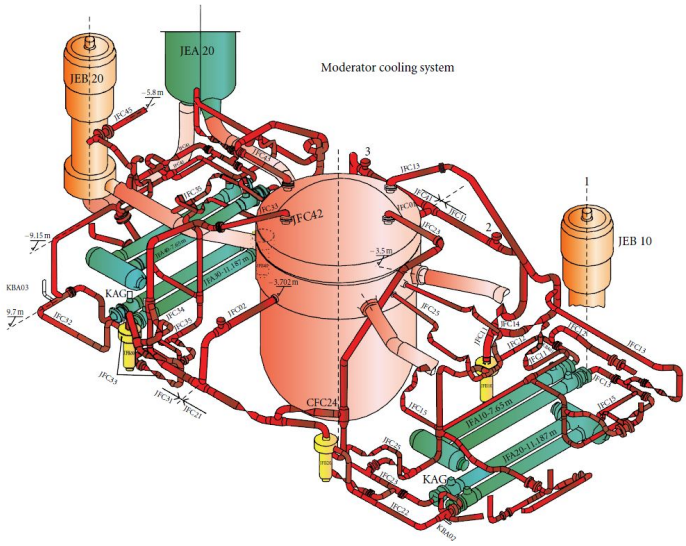

Figure 2. Moderator system layout (red pipes, yellow pumps and green coolers).

Under nominal conditions, the coolant Mass Flow Rate (MFR) is approximately 10540 Kg/s, and the inlet and outlet temperatures are 277°C and 314°C, respectively. The moderator MFR is 880 Kg/s, and the inlet and outlet temperatures are 140°C and 194°C, respectively. However, these temperatures can be varied (approximately 20%) to control reactivity. During full-load operation, 95% of the thermal power is generated by fission while the remaining 5% is generated by thermalization. Additionally, approximately 5% of the fission power is transferred from the coolant to the moderator. Therefore, this thermal power (approximately 220 MW) is used to pre-heat the steam-generators feed-water.

Atucha I and II are unique NPPs. Few research studies have been published; most of which were conducted with 0/1D codes to understand the thermo-hydraulic behaviour under postulated accidents (Lazarte et al. [2], Mazzantini et al. [3], and Bonelli et al. [1]). Even more unusual are the investigations based on Computational Fluid Dynamics (CFD) (Araneo et al. [4]).

CFD has become a valuable tool to analyse complex flows, and the nuclear industry is starting to use it for designing and assessing operations of safety systems. However, certain phenomena, such as two-phase heat transfer or turbulence, are not still fully understood. Therefore, the nuclear industry is rather cautious to use CFD for two-phase applications[5] [6]. Moreover, single-phase problems, such as natural convection, at extremely high Rayleigh Numbers (Ra) remain to be investigated, and a lack of information regarding the accuracy of the Boussinesq approach is found. Hence, before the moderator tank simulation is performed, a dedicated assessment of the CFD model was conducted.

This study is the third step in developing a model of the entire RPV considering the coolant and the moderator circuits. Two previous studies accounted for the in-core coolant flow assuming prescribed heat losses (Ramajo et al.[7], Corzo et al.[8]). This report is dedicated to estimating the heat transfer and the flow distribution inside the moderator tank.

2. Mathematical Formulation

In natural convection problems, the driving force is given by the density changes. Under certain conditions, the thermodynamic properties can be assumed as constants, adding a buoyancy body force (Boussinesq approximation) that couples the energy and the momentum equations. The mathematical background presented is based on the solver `buoyantBoussinesqPimpleFoam` from OpenFOAM 2.2.3 (Open Field Operation and Manipulation).

The continuity equation for a Newtonian incompressible single-phase can be expressed as follows:

$$\frac{\partial \mathbf{u_j}}{\partial x_j} = 0 \tag{1}$$

The momentum equation can be written as follows:

$$\frac{\partial \mathbf{u_j}}{\partial t} + \frac{\partial \mathbf{u_j u_i}}{\partial x_j} = -\frac{1}{\rho_0}\frac{\partial p}{\partial x_i} + \frac{1}{\rho_0}\frac{\partial}{\partial x_j}(\tau_{\mathbf{ij}} + \tau_{\mathbf{t,ij}}) + \frac{\rho}{\rho_0}\mathbf{g_i} \tag{2}$$

where $\mathbf{g}$ is the gravitational acceleration. The sub-index 0 corresponds to the reference values. τ_{ij} and $\tau_{t,ij}$ are the laminar and turbulent stress tensors, respectively. τ_{ij} can be expressed as follows:

$$\tau_{\mathbf{ij}} = \mu\left[\left(\frac{\partial \mathbf{u_i}}{\partial x_j} + \frac{\partial \mathbf{u_j}}{\partial x_i}\right) - \frac{2}{3}\left(\frac{\partial \mathbf{u_k}}{\partial x_k}\right)\delta_{ij}\right] \tag{3}$$

where μ is the molecular viscosity; and δ_{ij} is the Dirac tensor. By assuming $\mu = \mu_0$ and replacing Equation 3 in the momentum equation (Equation 2), we can obtain the expression as follows:

$$\begin{aligned}\frac{\partial \mathbf{u_j}}{\partial t} + \frac{\partial(\mathbf{u_j u_i})}{\partial x_j} &= -\frac{\partial}{\partial x_i}\left(\frac{p}{\rho_0} + \frac{2}{3}k\right) \\ +\frac{\partial}{\partial x_j}\left\{\nu_0\left[\left(\frac{\partial \mathbf{u_i}}{\partial x_j} + \frac{\partial \mathbf{u_j}}{\partial x_i}\right) - \frac{2}{3}\left(\frac{\partial \mathbf{u_k}}{\partial x_k}\right)\delta_{ij}\right] - R^D_{ij}\right\} &+ \mathbf{g_i}\left(1 + \frac{\rho - \rho_0}{\rho_0}\right)\end{aligned} \tag{4}$$

where $\nu_0 = \mu_0/\rho_0$; k is the turbulent kinetic energy; and R^D_{ij} is the deviatoric part of the Reynolds stress tensor. The last term in the right hand side is the buoyant term, which can be achieved using the Boussinesq approximation as follows:

$$\begin{aligned}\frac{\partial \mathbf{u_j}}{\partial t} + \frac{\partial(\mathbf{u_j u_i})}{\partial x_j} &= -\frac{1}{\rho_0}\frac{\partial p}{\partial x_i} \\ +\frac{\partial}{\partial x_j}\left\{\nu_{eff}\left[\left(\frac{\partial \mathbf{u_i}}{\partial x_j} + \frac{\partial \mathbf{u_j}}{\partial x_i}\right) - \frac{2}{3}\left(\frac{\partial \mathbf{u_k}}{\partial x_k}\right)\delta_{ij}\right]\right\} &+ \mathbf{g_i}\left[1 - \beta(T - T_0)\right]\end{aligned} \tag{5}$$

where $\nu_{eff} = \nu + \nu_t$ is the effective kinematic viscosity; and β is the volumetric expansion coefficient. An average constant value for β can be estimated as follows:

$$\beta = \frac{1}{V}\frac{\partial V}{\partial T} = \rho\frac{\partial}{\partial T}\frac{1}{\rho} \longrightarrow \overline{\beta} = \overline{\rho}\frac{\Delta\left(\frac{1}{\rho}\right)}{\Delta T} = \left(\frac{\rho_1 + \rho_0}{2}\right)\frac{\frac{1}{\rho_1} - \frac{1}{\rho_0}}{T_1 - T_0} \tag{6}$$

The incompressibility condition given by Equation 1 becomes a constraint for the pressure. Despite the fact that pressure does have not an explicit expression derived from the constitutive equations, it can be obtained by applying the divergence operator to the momentum equation, which leads to the Poisson equation.

Lastly, the set of governing equations can be completed using the energy equation, which can be formulated here in terms of temperature as follows:

$$\frac{\partial T}{\partial t} + \frac{\partial}{\partial x_j}(T\mathbf{u_j}) = \frac{\partial}{\partial x_k}\left(\alpha_{eff}\frac{\partial T}{\partial x_k}\right) + S_e \tag{7}$$

where S_e is a volume source and α_{eff} is the effective thermal diffusivity accounting for the molecular and turbulent diffusion as follows:

$$\alpha_{eff} = \frac{\nu_0}{Pr} + \frac{\nu_t}{Pr_t} \tag{8}$$

In Equation 8, Pr is the Prandtl number ($Pr = Cp\mu_0/\kappa$) and Pr_t is the turbulent Prandtl number ($Pr_t = Cp\mu_t/\kappa_t$), which is assumed to have a constant value of 0.7.

Based on the boundary condition in the energy equation, the lack of mesh refinement close to the walls is addressed by the Jayatilleke model, which locally modifies the thermal diffusivity based on a logarithmic law [9].

The turbulent closure equation is based on the Static Smagorinsky Large Eddy Simulation (LES) model[10], where the subgrid-scale eddy viscosity ν_t can be defined as follows:

$$\nu_t = C_S^2 \Delta^2 |\mathbf{S}| \tag{9}$$

where C_S is the Smagorinsky constant ($C_S \approx 0.2$), Δ is the length of the Sub-Grid Scale (SGS) eddies and $|\mathbf{S}|$ is the magnitude of the resolved strain rate tensor. Ferziger et al. [11] suggested that the parameter C_S has to be reduced or damped close to the walls. Thus, the largely used Van Driest damping function [12] can be selected to modify Δ as follows:

$$\Delta = \min\left(\Delta_{mesh}^{1/3}, \frac{\kappa'}{C_\Delta}\right)\left(1 - e^{-y^+/A^+}\right) \tag{10}$$

In Equation 10, Δ_{mesh} is the cell volume, $\kappa' = 0.4187$ is the von Kármán constant and $C_\Delta = 0.158$ is a model constant. The constant A^+ typically assumes a value of 26 [11]. y^+ is the dimensional distance from the wall ($y^+ = yu_\tau/\nu$), which is computed from the real distance (y) and the near-wall friction velocity (u_τ). $u_\tau = (\tau_w/\rho)^{1/2}$ is obtained from the wall shear stress (τ_w).

3. Code validation

Natural convection in closed domains has been extensively studied[13] [14] [15] by both numerical and experimental methods. However, there are few studies providing results close to the critical point, where the flow becomes unsteady. A more relevant parameter to characterize the intensity of the buoyant motion is the *Ra*, which can be defined as follows:

$$Ra = \frac{g\beta H^3 (T_h - T_c)}{\alpha\nu} \tag{11}$$

where H is a characteristic length; and $(T_h - T_c)$ is the maximum temperature difference inside the domain.

The Boussinesq approximation currently used for simulating industrial problems is valid if $\beta(T\text{-}T_{ref}) \ll 1$ [16]. For the current case (moderator tank), $\overline{\beta} = 0.0011[k^{-1}]$ and $\beta(T\text{-}T_{ref}) < 0.03$. However, the accuracy of this approach for modelling high *Ra* problems remains undecided in literature [17]. For industrial applications, like such as electric transformers, furnaces or nuclear reactors, the combination of a large H and high thermal gradients leads to an *Ra* value higher than 10^{10}. For these regimes, no experimental data can be found in the literature. The convective/conductive nature of the heat transfer can be analysed using the Nusselt Number (*Nu*) as follows:

$$Nu = \frac{hL}{\kappa} \tag{12}$$

where h is the convective heat transfer coefficient; and κ is the thermal conductivity.

The buoyancy-driven flow in a cubic or square cavity with adiabatic top and bottom walls is one of the most classical heat-transfer benchmarks [17]. It is often used for assessing numerical algorithms developed to solve incompressible recirculating flows [18]. At a low *Ra*, the 2D square cavity benchmark is suitable for code assessment. Thus, the widely known 2D numerical solutions given by De Vahl Davis [19] for $Ra=10^3$ to 10^6 can be used. This problem was analysed by the authors in a previous study [20], demonstrating the capability of OpenFOAM.

However, at high *Ra* values, the cubic cavity has to be used. The increase in complexity caused by the stronger coupling between the transport equations adds to the significant influence of the turbulence. It is well known that the Reynolds number (*Re*) is related to the *Ra* ($Re \propto Ra^{1/2}$) number. Therefore, this test allows us to determine the upper *Ra* beyond which the flow becomes unsteady. Paolucci and Chenoweth [21] and Le Quéré [18] studied this phenomenon and concluded that this point occurs at $Ra > 2x10^8$.

Literature data regarding high *Ra* benchmarks is scarce and limited to $Ra < 10^9$. The most relevant contributions arise from the numerical simulations performed by Le Quéré [18] ($Ra = 10^7$ and 10^8) and the experimental results achieved by Ampofo and Karayiannis[22] ($Ra = 1.59x10^9$) achieved with an air-filled cubic cavity. The same test was also performed by Tian and Karayiannis [23], who additionally obtained a large amount of data to estimate turbulence quantities. More recently, Peng and Davison [24] performed simulations of this problem. However, for the moderator tank, the *Ra* is higher than 10^{11}. Accordingly, only high *Ra* problems are included in this paper.

Solver settings in OpenFOAM. A pressure-based, segregated and transient solver was used. The Gauss Linear Upwind discretization was selected for the divergence terms. The PIMPLE algorithm was selected to perform the pressure-velocity coupling. Standard discretization based on Rhie and Chow [25] was selected for the pressure, and the Poisson equation was solved using the Gauss Linear scheme [24]. For the convergence criteria of the linear solver, an absolute residual below 10^{-6} or a relative reduction of three orders was required for all of the equations. For PIMPLE convergence, the momentum predictor was deactivated, and the outer corrections were not required while four inner corrections were performed. Non-orthogonal corrections were unnecessary despite the Cartesian grids used. Nevertheless, they were required for the moderator tank simulation. The turbulence model was achieved using the static Smagorisky model.

3.1. Cubic cavity results

The first part of this section is devoted to simulating the Ampofo and Karayiannis test. Then, an additional case for a higher *Ra* value was solved. Unfortunately, for this proposed case, no literature data are available for comparison.

The cubic cavity solved was 0.75 m high × 0.75 m wide × 1.5 m deep. To reproduce the Ampofo and Karayiannis, test the cavity was filled with air. The hot wall was kept at $T_h = 50°C$ while the cold wall was kept at $T_c = 10°C$. Two hexahedral structured meshes were evaluated; a coarse one with 127, 575 cells and a fine one with 702, 027 cells. Both were refined towards the walls. To compare the transient numerical result with the experimental data, time average solutions were obtained.

In Figure 3, the normalized vertical velocity (V) and the normalized temperature (θ) at the left end (hot wall) of the cavity mid-line are shown. A reasonably good agreement is observed, especially for the finer mesh despite the fact that the maximum y^+ was not sensibly reduced (the average value was changed from 4.6 to 3.8 to refine the mesh). In the cavity core (0.1 >X> 0.9), the velocity is almost negligible, and the temperature hold is nearly constant, indicating the existence of a stagnant flow zone. With the finer mesh, a better agreement near the wall is obtained for the velocity. The overestimation also predicted by Pen and Davison [24] is not found.

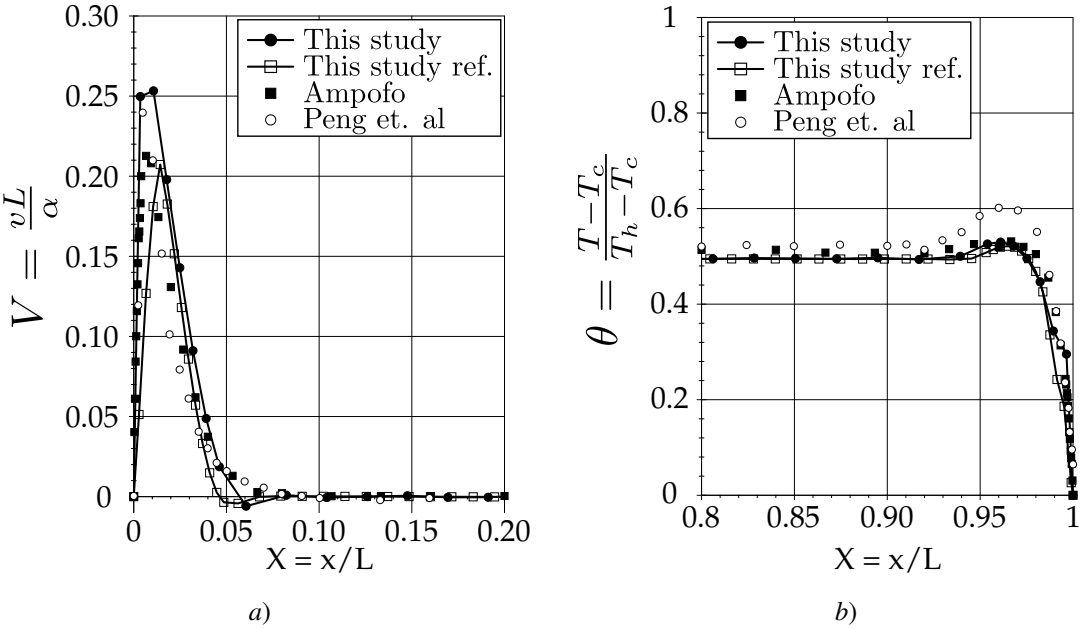

Figure 3. Cubic cavity test for $Ra = 1.59x10^9$, Mid-line ($Y = 0.5$, $Z = 0.5$) transport properties: a) Normalized vertical velocity (V); and b) Normalized temperature (θ)

To achieve an extremely high *Ra* value ($Ra = 4.1 \times 10^{11}$), the cubic cavity was filled with water ($Pr = 5.42$), thus conserving the same wall temperature setting. Due to convergence stability requirements, the problem was solved using a very fine structured mesh of 3, 243, 375 hexahedral cells. For this mesh, the maximum and the average y^+

were 14.7 and 8.7, respectively. A total time of 1000s was solved and a mean solution was obtained by taking a time-average of the last 500s.

The transport variables (V and θ) in the horizontal mid-line are presented in Figure 4. Eleven time solutions are included along with the averaged one. It should be noted that in the cavity core, the velocity is continuously changing around the zero value while the temperature holds nearly constant. A strong velocity and temperature gradients can be observed close to the walls.

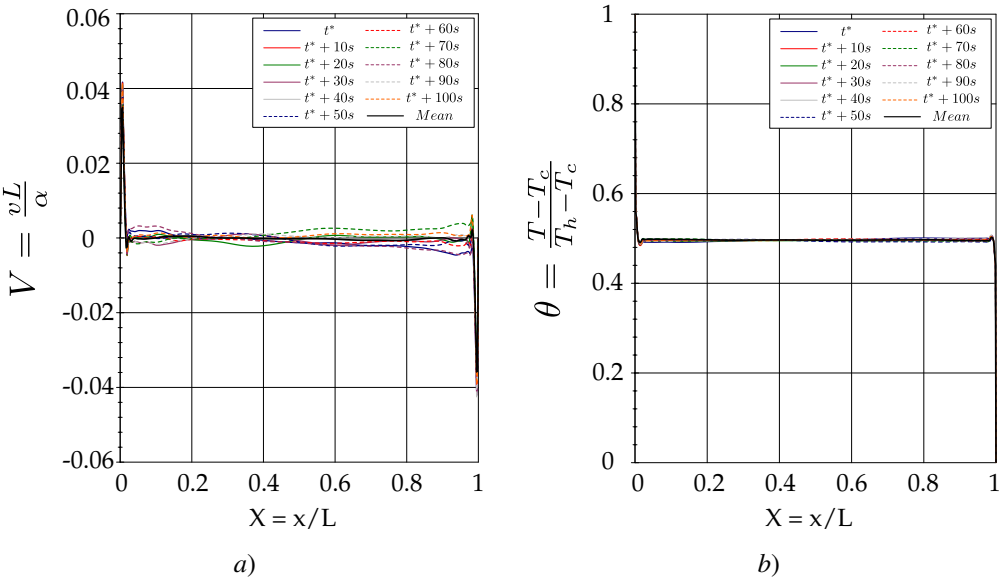

Figure 4. Cubic cavity test for $Ra = 4.1x10^11$, Mid-line ($Y = 0.5$, $Z = 0.5$) transport properties: a) Normalized vertical velocity (V); and b) Normalized temperature (θ)

Figure 5 illustrates the temperature distribution for four different Ra values (10^3 10^6 $1.59x10^9$ and $4x10^{11}$). Although the two upper pictures correspond to previously reported results for very low Ra values, they were included to note the evolution of temperature as Ra increased. It can be concluded that in those problems, convection dominated over conduction (high Nu and Ra) and a characteristic thermal stratification in the vertical direction was observed.

4. Moderator tank

4.1. Constructive and operative characteristics

As mentioned above, the moderator tank is vertically crossed by 451 CCs. To reduce the coolant heat loss, each CC is covered by a corrugated thin foil sheet, which has orifices to allow the moderator to fill the gap between it and the outer wall of the CC. Despite the orifices, the heat transferred from the CCs is estimated to be approximately 112 MW. However, the heat generated by thermalization is estimated to be approximately 108 MW. The resulting 220 MW represents more than 10% of the total thermal power.

In addition to the CCs, the moderator tank houses nine hafnium absorbers rods, corresponding to the first fast shut down system, four fast boric injection lances composing the second fast shut down system and nine steel rods for reactivity control. These rods and lances cross the tank diagonally while passing across the swarm of CCs with inclination angles ranging from 20° to 25°. All of these parameters were included in the previous simulations [26] and demonstrated a negligible effect on the overall flow behaviour. Hence, they were removed in the current model with the goal of using hexahedral structured cells for meshing.

Figure 6 provides the details of the lower distributor ring. It is symmetric with respect to a meridional vertical plane dividing the ring in two parts. Each part is composed of two isolated quadrants with an inlet downcomer and a set of mouthpieces and orifices for the flow discharge. Each quadrant has 16 mouthpieces placed at the bottom

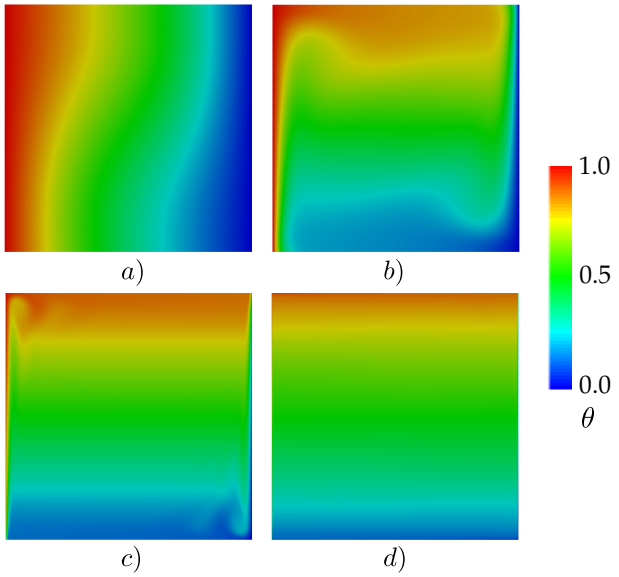

Figure 5. Normalized temperature field $\theta = \frac{T-T_c}{T_h-T_c}$; a) $Ra = 10^3$; b) $Ra = 10^6$; c) $Ra = 1.59x10^9$; and d) $Ra = 4.1x10^{11}$

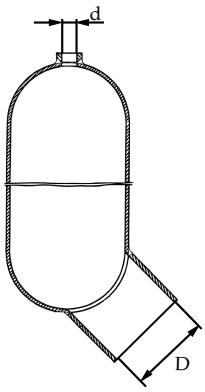

	Quadrant 1					Quadrant 4				
	d/d_1	MFR[kg/s]	D/D_1	MFR[kg/s]		d/d_1	MFR[kg/s]	D/D_1	MFR[kg/s]
1	d_1	1.511	D_1	12.138	1	1.042	1.633	1	12.750
2	1	1.503	1	12.298	2	1.042	1.583	1	12.788
3	1	1.523	1	12.005	3	1.042	1.558	1	12.496
4	1	1.473	1.015	11.421	4	1.042	1.539	1.015	12.313
5	1	1.481	1.136	14.098	5	0.945	1.490	1.272	12.172
6	0.953	1.342	1.621	16.993	6	0.903	1.422	1.030	11.588
7	0.953	0.933	1.1061	9.7565	7	0.852	1.415	1.030	11.031
8	1	1.239	1.060	10.321	8	0.878	1.408	1.030	10.133
9	1.050	1.439	1.030	10.534	9	1.042	1.423	1.030	9.7762
10	1.050	1.444	1.030	11.248	10	1.042	0.970	1.030	8.6844
11	1.050	1.500	1.030	11.844	11	1.042	0.792	1.030	12.584
12	1.050	1.530	1.030	12.221	12	1.042	1.168	1.030	17.300
13	1.050	1.583	1.030	12.381	13	1.042	1.326	1.030	11.505
14	1.050	1.598	1.030	12.741	14	1.042	1.432	1.030	11.974
15	1.050	1.647	1.030	12.794	15	1.042	1.624	1.030	12.273
16	1.050	1.649	1.030	12.875	16	1.042	1.612	1.030	12.542
17	1.050	1.655			17	1.042	1.648		
18	1.050	1.638			18	1.042	1.656		

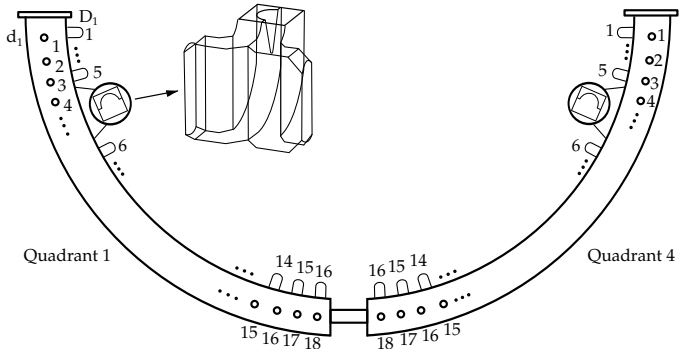

Figure 6. Orifices and mouthpieces in two of the four quadrants of the distributor ring.

oriented 45° towards the centre of the tank floor and 18 orifices placed at the top vertically oriented to the top of the tank.

The mouthpieces are larger than the orifices, and all of them have different diameters. Moreover, the azimuth distribution is not homogeneous. The table included in Figure 6 presents the ratio d/d_1 for the orifices and D/D_1 for the mouthpieces. d_1 and D_1 are the diameters of the first orifice and the first mouthpiece of quadrant 1, respectively. The ratio D_1/d_1 is 4.71.

Each inlet downcomer is connected to the quadrant by an elbow. Because the elbow is not in the middle of the quadrant, a flow deflector is placed inside it to drive most of the flow towards the larger side (see the detail in Figure 6). There are no mouthpieces or orifices near the elbows. Therefore, the diameters of mouthpieces 5 and 6 are larger than those of the others to achieve a homogeneous flow.

In contrast with the complexity of the distributor, the collector ring is only divided into two isolated parts, and each one is connected to an outlet duct. The ring has 88 orifices with different diameters and azimuth separations.

4.2. Computational model

A full 3D model was solved under nominal conditions. Single-phase, non-isothermal simulations were conducted considering the fission heat transferred from the CC walls and the heat generated by the neutron thermalization. Figure 7 provides the developed computational model. The different colours of the CCs correspond to the five hydraulic zones (HZ) in which the core is divided. Each HZ has different fission power and consequently different coolant flows. The central zone (HZ 5) has 253 CCs and approximately %70 of the total thermal power. Details on the amount of CCs per HZ are provided in Table 1.

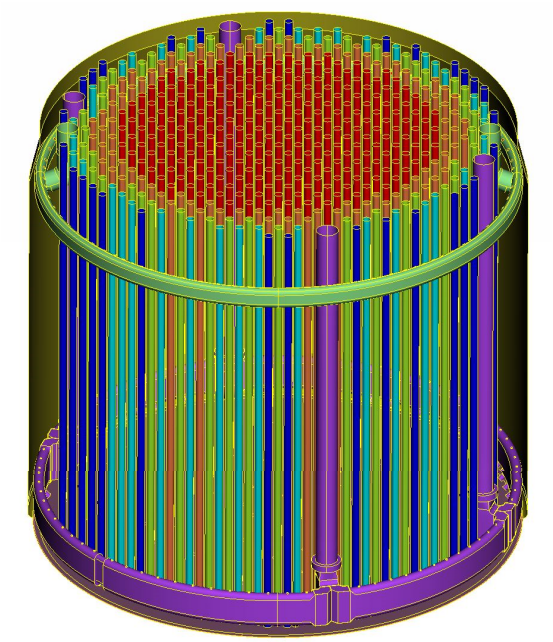

Figure 7. View of the computational model; the colours of the CCs indicate the different HZs.

The moderator inlet flow was homogeneously shared in the four downcomers, and the flow was solved inside the distributor ring. However, the flow inside the collector ring was not solved but a homogeneous outlet static pressure (115 bar) was imposed on the orifices. The overall computational model of the moderator tank was discretized with 41, 686, 659 cells. The central core of the tank was meshed with structured hexahedral cells while tetrahedral cells were used around the periphery. Figure 8 provides the details of the mesh. A significant refinement was necessary inside the elbows and close to the orifices and mouthpieces. A dedicated refinement was performed around the CCs

using four layers to mesh the first 15 mm close to the CC walls. The use of layers allowed the thickness of the first element to be reduce to only 3 mm, thus obtaining an average $y^+ < 180$.

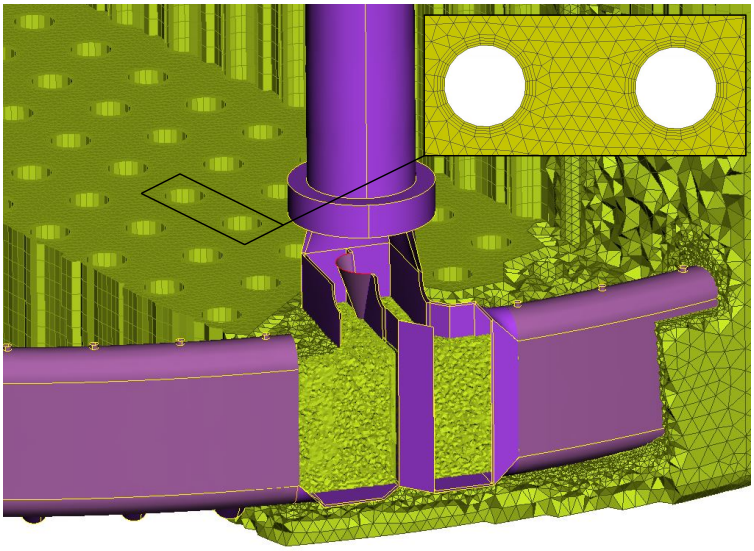

Figure 8. View of the hybrid mesh around the distributor ring.

The governing equations were solved using the same solver and set up as described in the validation test section. The calculations were performed using adjustable time step criteria by keeping the maximum Courant less than 5. Distributed shared memory parallel computing in a Beowulf cluster (Intel-i7-2600K, 3.40GHz, and 16 GB RAM) was used. Twenty-four processors shared in 6 cluster nodes were necessary to allocate the case.

A set of polynomial functions were implemented to model the thermodynamic properties of heavy water by fitting the NIST[27] database for a pressure range from 94 to 130 bar and temperatures ranging from 130 to 200°C as follows:

$$\rho(p,T) = 979.3 - 0.5817p + 1.286T + 0.00223p^2 + 0.000763pT - 0.006267T^2 [kg/m^3] \quad (13)$$

$$\mu(p,T) = 0.0003899 - 2.007\times10^{-8}p - 1.601\times10^{-6}T + 1.142\times10^{-10}p^2 - 1.954\times10^{-10}pT + 2.08\times10^{-9}T^2 [Pas] \quad (14)$$

$$Cp(T) = 4.583\times10^4 - 732T + 4.8T^2 - 0.01392T^3 + 1.519\times10^{-5}T^4 [J/kgk] \quad (15)$$

4.3. Thermal coupling between moderator and coolant

The thermal boundary conditions deserve special attention. The overall heating power in the moderator is prescribed from the plant design. However, no any measure value is available for comparison. Due to the importance of the convective/conductive heat transfer from the coolant to the moderator, additional effort was dedicated to developing a suitable method for coupling the 3D moderator tank model with an in-house 1D code for modelling the CCs. This 1D code solves the single-phase transport momentum and energy equations using volume finite methods and a pseudo-compressible formulation. Details on the implementation are out of the scope of the current study but can be found in Corzo et. al [8] and Corzo [28]. To achieve the coupling between the 3D CFD and the 1D code, a 2D heat transfer model was developed. This model considers the convection between the coolant and the inner side wall of the CCs, conduction along the CC wall, convective/conductive transfer across the gap between the CCs and the foils, conduction along the foil sheet and convective transfer between the foil and the moderator. By considering all of these thermal resistances, the effective conductivity κ_{tot} can be written in cylindrical coordinates as follows:

$$\kappa_{tot} = \frac{\pi}{\frac{1}{h_{cc}d_1} + \frac{ln\left(\frac{d_1}{d_2}\right)}{2\kappa_z} + \frac{ln\left(\frac{d_3}{d_2}\right)}{2\kappa_a} + \frac{ln\left(\frac{d_4}{d_3}\right)}{2\kappa_z} + \frac{1}{h_{mod}d_4}} \tag{16}$$

where d_1 and d_2 are the internal and the external diameters of the CC tube, respectively; d_3 and d_4 are the internal and the external diameters of the foil, respectively (see the left side of Figure 10); h_{cc} and h_{mod} are the convective coefficients between the coolant and the CC walls and the foils and moderator, respectively; κ_z is the thermal conductivity of zircaloy (κ_z = 13.6 W/mk); and κ_a is an equivalent heat transfer conductivity, which accounts for the convection/conduction across the D_2O gap.

h_{cc} can be estimated using the equation as follows:

$$h_{cc} = \frac{Nu\ \kappa_{cc}}{D_h} \tag{17}$$

where κ_{cc} is the coolant conductivity (κ_{cc} = 0.4855 W/mk for a mean temperature of 295°C); and D_h is the hydraulic diameter of the CC ($D_h = 9.48 \times 10^{-3}$ m). Nu can be estimated using the Dittus-Boelter equation for a single-phase internal turbulent flow as follows:

$$Nu = 0.023\left(\frac{GD_h}{\mu}\right)^{0.4}\left(\frac{\mu Cp}{\kappa_{cc}}\right) \tag{18}$$

where G is the coolant mass flux. For the heat transfer across the D_2O gap, the conduction is poorly enhanced by the low fluid motion induced by the natural convection within the gap. For fluids confined between vertical flat plates, the correlation can be recommended [29] as follows:

$$\frac{\kappa_a}{\kappa_{gap}} = 1 + \frac{0.119(GrPr)^{1.27}}{GrPr + 1.45 \times 10^4} \tag{19}$$

where Gr is the Grashof number, which can be expressed as follows:

$$Gr = \frac{g\beta(T_w - T_\infty)L^3}{\nu^2} \tag{20}$$

In Equation 20, κ_{gap} is the thermal conductivity of the moderator in the gap, which, for simplicity, is assumed to be equal to κ_{cc}; L is the CC length (L = 6.122 m); T_w is the temperature of the outer foil wall; and T_∞ is the bulk temperature. Because all of the HZ's have a similar coolant temperature profile, the same κ_a value ($2.44 W/mk$) was used. Lastly, the convection coefficient h_{mod} can be estimated as follows:

$$h_{mod} = \kappa_M(GrPr)^{1/3}\frac{\kappa_{cc}}{D_h} \tag{21}$$

where κ_M is the equivalent thermal conductivity (κ_M = 0.13). Once the effective thermal conductivity κ_{tot} is estimated from Equation 16, the heat flux in each CC can be calculated as follows:

$$q_l(x, HZ) = \kappa_{tot}L[T_{cc}(x, HZ) - T_{mod}(x, HZ)] \tag{22}$$

where T_{cc} and T_{mod} are the coolant and the moderator temperature profiles, respectively. Once $q_l(x, HZ)$ is obtained, the outer foil wall temperature T_w can be easily estimated as follows:

$$T_w(x, HZ) = \frac{q_l(x, HZ)}{h_{mod}} + T_{mod}(x, HZ) \tag{23}$$

The moderator temperature $T_{mod}(x, HZ)$ is a priori unknown. Moreover, the coolant temperature $T_{cc}(x, HZ)$ is a function of the heat loss and the fission power distribution, which is different for each HZ. Therefore, an iterative step-wise procedure must be conducted. The algorithm can be summarized as follows:

Algorithm 1 : `2D thermal coupling procedure`

1. An 1D estimation for the coolant temperature $T_{cc}(x, HZ)$ is obtained from the CC-1D code by assuming that the heat loss is equal to 5% of the fission power.
2. A constant moderator temperature ($T_{mod}(x, HZ) = 180°C$) is assumed and $q_l(x, HZ)$ is obtained.
3. The 3D CFD model of the moderator tank is solved using $q_l(x, HZ)$.
4. Some temperature profiles ($T_{mod}(x, HZ)$) along selected vertical lines (one for each HZ) are extracted from the solution.
5. $q_l(x, HZ)$ is updated with the new $T_{mod}(x, HZ)$.
6. $T_w(x, HZ)$ is calculated from Equation 23.
7. Gr (Equation 23) is calculated by taking $T_\infty = T_{mod}(x, HZ)$.
8. h_{mod} is updated (Equation 21).
9. κ_{tot} is updated (Equation 16).
10. Steps 4 to 8 are repeated until the variation in $q_l(x, HZ)$ becomes negligible.
11. The process starts again from step 3 with the new $q_l(x, HZ)$.

The iterative procedure is finalized once the T_{mod} obtained in step 4 shows no significant variation with respect to the previous values. At this point, it is necessary to repeat the overall algorithm by returning to step 1, updating $T_{cc}(x, HZ)$ and starting again.

In the current model, the 1D code for the CCs, 2D code for heat transfer and 3D CFD model are staggered solved. Nonetheless, convergence is quickly achieved after a few external loop iterations.

The wall boundary condition $q_l(x, HZ)$ was implemented using the `turbulentHeatFlux Temperature` BC in OpenFOAM. This BC is particularly useful for industrial problems for which the near wall refinement required by others BC (e.g., fixed temperature wall) is hard to achieve. This BC can be reconstruct the temperature gradient by considering the effective thermal diffusivity α_{eff} near the wall as follows:

$$\nabla T = \frac{q_l(x, HZ)}{\rho_0 C p_0 \alpha_{eff}} \tag{24}$$

The in-core power distribution in Atucha II has been studied by other authors using neutron kinetic models. This exceeds the scope of the current study. Hence, a volumetric energy source was estimated based on the neutron-flux results reported by Mazzantini et al. [3] along with the mean axial fission power distribution also used for solving the 1D-CC flow [8]. Figure 9 illustrates the resulting thermal power by neutron thermalization.

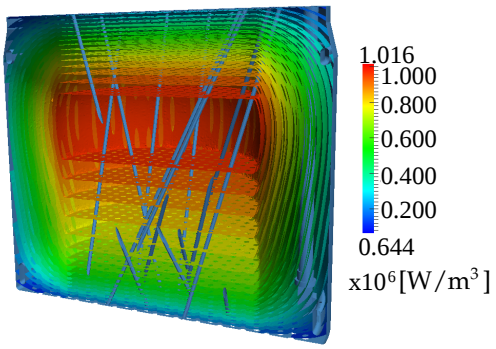

Figure 9. Iso-surfaces of the moderation power S_e.

4.3.1. Moderator tank Results and Discussion

Figure 10 can help visualize the heat transfer from the coolant to the moderator. A sketch is shown on the left side. On the right side, the temperature profile results rising from the thermal coupling are displayed. The figure depicts the temperatures for the coolant (Position 1), outer CC wall (Position 2), foil (Position 3) and moderator bulk. The large temperature jump across the CC-foil gap should be noted. Despite the different mass flows, the temperature differences between the coolant (Position 1) and the CC walls (Position 2) are nearly the same for all of the *HZ*'s.

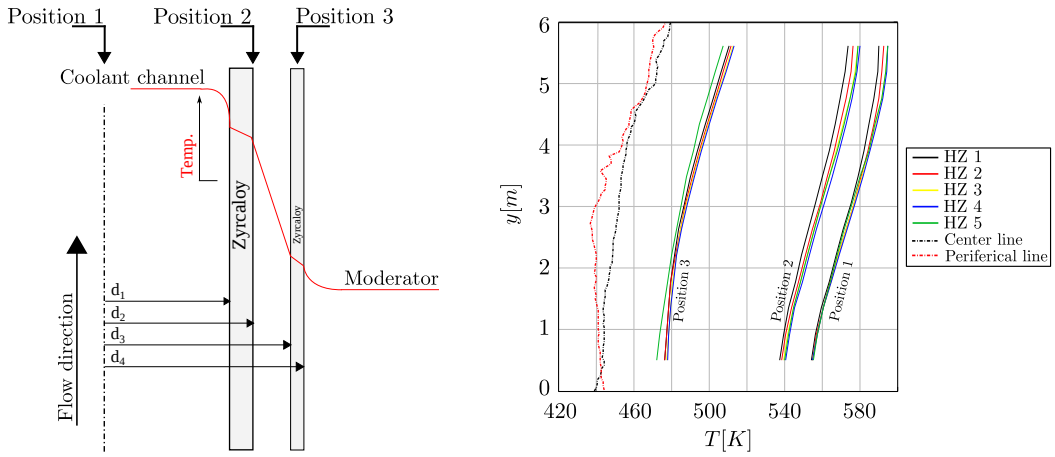

Figure 10. Heat transfer from the coolant to the moderator: Left) Radial heat transfer model; Right) Temperature profiles of the coolant and the outer side of the foils covering the CCs.

The overall thermal power transferred from each HZ is obtained by integrating Equation 22 along the x-coordinate. Table 1 reports these results; the first column is the HZ, and the second column is the amount of CCs per HZ. The third column is the average heat power transferred by one CC, and the fourth column is the ratio between the heat loss and the fission power of one CC. It should be noted that each HZ has considerably different results. Lastly, the fifth column is the total heat loss per HZ. The total heat power transferred from the coolant to the moderator can be obtained by summing the last, thus equalling 98.41 MW. This value is less than expected from the design and represents approximately 4.5% of the total thermal power. As noted, all of the CCs have similar heat loss even though the central CCs have three times more fission power than the most peripheral one. This results can be explained by two reasons: first, the coolant temperature profiles are similar for all of the *HZ*'s (as indicated in Figure 10). Secondly, the convective coefficient h_{cc} has a poor incidence (which increased with the coolant mass flow), i.e., the conduction/convection mechanism. In this case, the high thermal resistance of the CC-foil gap dominates over the other terms.

HZ	Chan.	q_{loss} (MW)	$q_{loss}/q_{fiss}(\%)$	q_{tot} (MW)
1	30	0.212	10.9	6.360
2	36	0.217	8.1	7.812
3	42	0.219	6.0	9.198
4	90	0.221	4.4	19.89
5	253	0.218	3.4	55.15

Table 1. Heat transfer power from the CCs to the moderator.

The left side of Figure 11 depicts the MFR across the mouthpieces and the orifices in the quadrants 1 and 4. For

the mouthpieces the flow distribution is quite symmetric, demonstrating the highest MFR near the elbows. However, the other hand, the flow through the orifices is more homogeneous. The entering jets coming from the mouthpieces and the orifices are illustrated on the right side of Figure 11. A view from the top is displayed in the top view. It can be observed how the different jets penetrate into the CC bunch without reaching the centre.

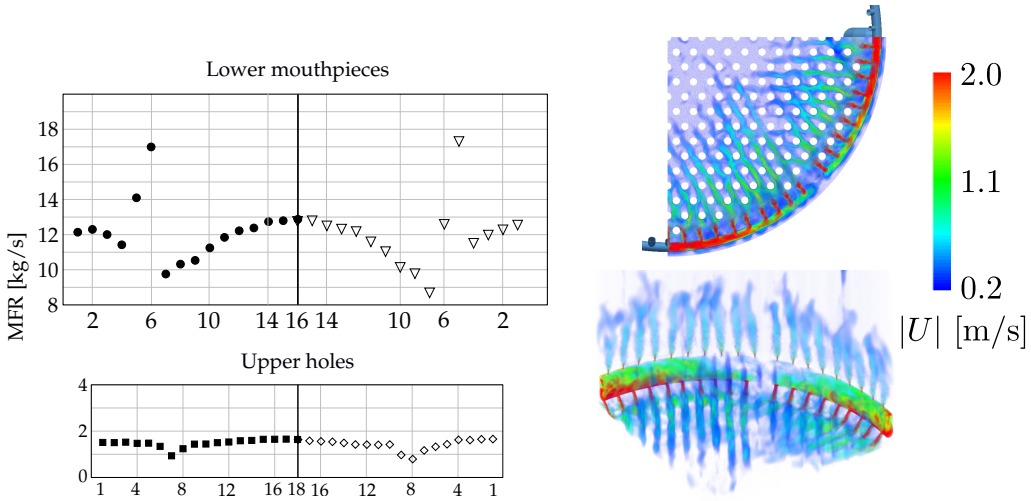

Figure 11. Inlet flow from the distributor ring: Mass flow in the orifices and the mouthpieces, Velocity map field clipped by [0.2-2]m/s

The temperature pattern over one vertical plane cutting the moderator tank is provided in Figure 12. The results were obtained by averaging over a time window of 800 s. As noted, the inlet flow orientation has a significant incidence on the thermal field but a typical stratification in the vertical direction that characterizes the natural convection found in high *Ra* problems. Although the driving force is both natural and forced convection, the entering flow only has a local influence on the overall thermal pattern.

Temperature differences greater than 70K are found between the lower and the upper side of the tank. However, this result is expected despite the inlet and outlet temperatures and the low mixing of the flow. The zone below the dotted-line is characterized by lower temperatures because of the penetration of the inlet flow. Similarly, the flow coming from the orifices promotes a cold zone around the periphery of the tank.

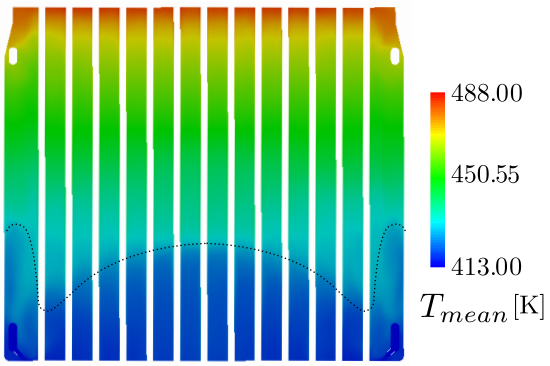

Figure 12. Temperature field over a mid vertical plane.

In Figure 13 the temperature is visualized over four horizontal cut planes; the first one is placed just below the distributor ring. The effect produced by the jets coming from the mouthpieces and how they penetrate inside the CC bunch should be noted. Plane 2 is located just above the distributor ring. A slightly radial stratification is evidenced

by a core that is cooler than the periphery. The opposite effect is indicated in plane 3 (located at 0.35 of the total tank height). However, in the top of the tank above the collector ring (plane 4), the temperature becomes more homogeneous with a few local cold and hot spots. Nevertheless, in all of the planes, the temperature difference remains less than 20K.

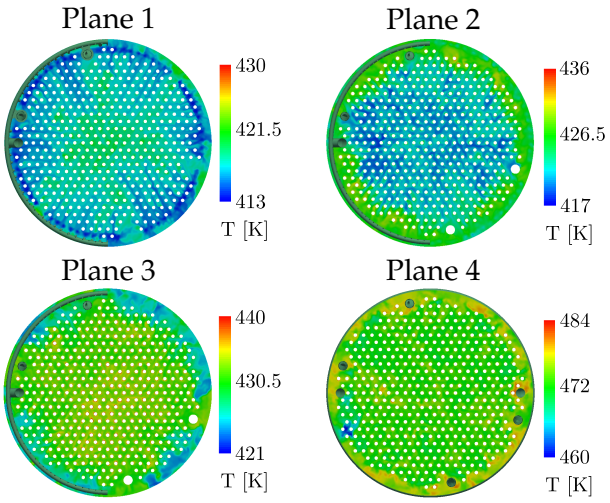

Figure 13. Temperature in horizontal planes.

5. Conclusions

A full 3D simulation of the moderator tank of a PHWR was performed using CFD. First, the *buoyantBoussinesqPimpleFoam* solver was assessed for a range of high *Ra* values. Suitable thermal boundary conditions accounting for the heat transferred from the coolant were obtained using an in-house 1D code for solving the in-channel flow. The results concluded that all of the coolant channels transfer nearly the same thermal power, despite the fact that the fission heat is three times larger at the centre than that at the periphery of the reactor. This result is due to the high thermal resistance imposed by the CC-foil gaps. The temperature differences along the vertical direction can be attributed to the low mixing and the orientation of the entering cold flow. However, the thermal stratification in the radial direction is less significant (20K). The results seem to be as expected for extremely high *Ra* systems.

Acknowledgements

The authors would like to thank the Universidad Nacional del Litoral (CAI+D 2011 PJ 500 201101 00015 and CAI+D PI 501 201101 00435), CONICET (PIP 112 201101 00331) and ANPCyT (PICT 2013-830). Additionally, they would like to thank Autoridad Regulatoria Nuclear (ARN) for its financial and technical support. Lastly, thanks should be given to Nicolas Schiliuk, who contributed significantly to improving this study.

References

[1] A. Bonelli, O. Mazzantini, M. Sonnenkalb, M. Caputo, J. M. García, P. Zanocco, M. Gimenez, Station black-out analysis with melcor 1.8. 6 code for atucha 2 nuclear power plant, Science and Technology of Nuclear Installations 2012.

[2] A. I. Lazarte, W. Fullmer, M. Bertodano, Experimental validation of relap5 and trace5 for licensing studies of the boron injection system of atucha ii, Science and Technology of Nuclear Installations 2011.

[3] O. Mazzantini, M. Schivo, J. Di Césare, R. Garbero, M. Rivero, G. Theler, A coupled calculation suite for atucha ii operational transients analysis, Science and Technology of Nuclear Installations 2011.

[4] D. Araneo, P. Ferrara, F. Moretti, A. Rossi, A. Latini, F. D'Auria, O. A. Mazzantini, Integrated software environment for pressurized thermal shock analysis, Science and Technology of Nuclear Installations 2011.
[5] J. Mahaffy, B. Chung, C. Song, F. Dubois, E. Graffard, F. Ducros, M. Heitsch, M. Scheuerer, M. Henriksson, E. Komen, et al., Best practice guidelines for the use of cfd in nuclear reactor safety applications, Tech. rep., Organisation for Economic Co-Operation and Development, Nuclear Energy Agency-OECD/NEA, Committee on the safety of nuclear installations-CSNI, Le Seine Saint-Germain, 12 boulevard des Iles, F-92130 Issy-les-Moulineaux (France) (2007).
[6] J. Mahaffy, Development of best practice guidelines for cfd in nuclear reactor safety, Nuclear Engineering and Technology 42 (4) (2010) 377–381.
[7] D. Ramajo, S. Corzo, N. Schiliuk, N. Nigro, 3d modeling of the primary circuit in the reactor pressure vessel of a phwr, Nuclear Engineering and Design 265 (2013) 356–365.
[8] S. Corzo, D. Ramajo, N. Nigro, 1/3d modeling of the core coolant circuit of a phwr nuclear power plant, Annals of Nuclear Energy 83 (2015) 386–397.
[9] C. Jayatilleke, The influence of prandtl number and surface roughness on the resistance of the laminar sub-layer to momentum and heat transfer, Ph.D. thesis, University of London (1966).
[10] J. Smagorinsky, General circulation experiments with the primitive equations. 1.the basic experiment, Mon. Weather Rev. 91 (1963) 99–164.
[11] J. H. Ferziger, M. Peric, Computational methods for fluid mechanics, Chapter 5 (2002) 85–127.
[12] E. R. Van Driest, On turbulent flow near a wall, Journal of the Aeronautical Sciences (Institute of the Aeronautical Sciences) 23 (11).
[13] J. Patterson, J. Imberger, Unsteady natural convection in a rectangular cavity, J. Fluid Mech 100 (1) (1980) 65–86.
[14] J. Salat, S. Xin, P. Joubert, A. Sergent, F. Penot, P. Le Quere, Experimental and numerical investigation of turbulent natural convection in a large air-filled cavity, International journal of heat and fluid flow 25 (5) (2004) 824–832.
[15] H. Dixit, V. Babu, Simulation of high rayleigh number natural convection in a square cavity using the lattice boltzmann method, International journal of heat and mass transfer 49 (3-4) (2006) 727–739.
[16] W. L. Gustafsson, AM, G. Hellström, Cfd-modelling of natural convection in a groundwater-filled borehole heat exchanger, Applied Thermal Engineering 30 (2010) 683–691.
[17] A. Baïri, E. Zarco-Pernia, J. , García De María, A review on natural convection in enclosures for engineering applications. the particular case of the parallelogrammic diode cavity, Applied Thermal Engineering 63 (1) (2014) 304–322.
[18] P. Le Quéré, Accurate solutions to the square thermally driven cavity at high rayleigh number, Computers & Fluids 20 (1) (1991) 29–41.
[19] G. De Vahl Davis, Natural convection of air in a square cavity: a bench mark numerical solution, International Journal for Numerical Methods in Fluids 3 (3) (1983) 249–264.
[20] S. Corzo, S. Damián, D. Ramajo, N. Nigro, Numerical simulation of natural convection phenomena, Mecánica Computacional 30 (2011) 277–296.
[21] S. Paolucci, D. Chenoweth, Transition to chaos in a differentially heated vertical cavity, J. Fluid Mech 201 (1989) 379–410.
[22] F. Ampofo, T. Karayiannis, Experimental benchmark data for turbulent natural convection in an air filled square cavity, International Journal of Heat and Mass Transfer 46 (19) (2003) 3551–3572.
[23] Y. Tian, T. Karayiannis, Low turbulence natural convection in an air filled square cavity:: Part i: the thermal and fluid flow fields, International Journal of Heat and Mass transfer 43 (6) (2000) 849–866.
[24] S. Peng, L. Davidson, Numerical investigation of turbulent buoyant cavity flow using large eddy simulation, in: Int. Symp. Turbulence Heat Mass Transfer, Vol. 3, 2000, pp. 737–744.
[25] C. Rhie, W. Chow, Numerical study of the turbulent flow past an airfoil with trailing edge separation, AIAA 21.
[26] D. Ramajo, S. Corzo, N. Schiliuk, A. Lazarte, N. Nigro, Cfd modeling of the moderator tank of a phwr nuclear power plant, Mecánica Computacional 33 (2014) 2913–2926.
[27] Y. Ralchenko, A. Kramida, J. Reader, Nist atomic spectra database (version 4.0), National Institute of Standards and Technology, Gaithersburg, MD.
[28] S. Corzo, Assessment of nuclear power reactor using computational fluid dynamics, Ph.D. thesis, Universidad Nacional del Litoral (UNL), http://www.cimec.org.ar/ojs/index.php/cimec-repo (2015).
[29] T. Köble, F. Meyer, M. Ockenfels, J. Weltz, W. Von Witsch, G. Wollmann, The influence of convection on high-pressure gas target densities, Nuclear Instruments and Methods in Physics Research Section A: Accelerators, Spectrometers, Detectors and Associated Equipment 275 (2) (1989) 460–461.